

See discussions, stats, and author profiles for this publication at: <https://www.researchgate.net/publication/231376873>

Parametric Study of Gasification Processes in a BFB Coal Gasifier

ARTICLE *in* INDUSTRIAL & ENGINEERING CHEMISTRY RESEARCH · APRIL 2011

Impact Factor: 2.59 · DOI: 10.1021/ie1023029

CITATIONS

13

READS

43

3 AUTHORS:



[L.M. Armstrong](#)

University of Southampton

13 PUBLICATIONS 132 CITATIONS

SEE PROFILE



[Sai gu](#)

Cranfield University

95 PUBLICATIONS 2,120 CITATIONS

SEE PROFILE



[K. H. Luo](#)

University College London

129 PUBLICATIONS 1,534 CITATIONS

SEE PROFILE

Parametric Study of Gasification Processes in a BFB Coal Gasifier

L. M. Armstrong,[†] S. Gu,^{*,†,‡} and K. H. Luo[†]

[†]Energy Technology Research Group, School of Engineering Sciences, University of Southampton, Southampton SO17 1BJ, United Kingdom

[‡]Xi'an Jiaotong-Liverpool University, No.111 Ren'ai Road, Suzhou Dushu Lake Higher Education Town, Suzhou 215123, China

ABSTRACT: An Eulerian-Eulerian computational fluid dynamics (CFD) model of the gasification processes in a coal bubbling fluidized bed (BFB) is presented based on the experimental setup taken from the literature. The base model is modified to account for different parameter changes in the model setup. The exiting gas compositions for the base model have been averaged over time and validated with experimental data and compared to the exiting results for the different parameter models. An extensive study is also carried out which considers the variation of different parameters such as bed temperatures, bed height, bed material, heat transfer coefficients, and devolatilization models influenced the gasification processes in different ways. Such an extensive parametric study has yet to be carried out for an Eulerian-Eulerian coal gasification model.

INTRODUCTION

Recent environmental concerns with regards to increased greenhouse emissions has prompted the search for cleaner coal thermal conversion technologies. Ensuring a more efficient burn out of the fuel is one step closer to achieving this. Bubbling fluidized bed gasifiers (BFBG) are widely utilized in industry due to their excellent mixing properties and high residence times leading to a more efficient gasification process. The experimental determination of optimal gasification conditions including the addition of catalysts, e.g. limestone, to reduce harmful emissions is expensive. A computational fluid dynamic (CFD) model capable of predicting such emissions would be highly beneficial.

CFD modeling has shown to be a viable tool for the simulation of complex gas–solid flows and heat transfer processes that take place in fluidized bed technologies (FBT). Yet the incorporation of the complex species transport equations and reactions within the models have been very limited due to the high computational cost. However, the increase in computer performance and capabilities in recent years allows for such complex models to be carried out. The incorporation of gasification reactions into Eulerian-Eulerian two-fluid modeling (TFM) has only recently been considered since research continues to focus on the improvement of the basic gas–solid flow models and rheologies. Yet the authors feel that current models display reasonable enough results to consider the incorporation of species and reaction modeling especially since the slight improvements that could be obtained through the modification of such gas–solid flow models; e.g. drag models; would not greatly affect the reaction rates and species release of the gaseous products.

TFM is the most frequently applied method for the gas–solid flow^{1–6} and heat transfer modeling^{7–10} within FBT as it assumes the gas and solid phases as continuous and fully interpenetrating within each control volume. It is less computationally exhaustive in comparison to the Eulerian-Lagrangian method which simulates the individual particle dynamics.^{11–13} A combination of the Eulerian-Eulerian model and the Eulerian-Lagrangian model was considered looking into the flow dynamics, heat transfer, and reaction kinetics of one or two Lagrangian biomass particles interacting with an Eulerian-Eulerian bubbling bed of inert sand.^{14–22} Although this

approach is highly beneficial for the investigation at an individual particle dynamic scale, the simulation was limited to up to 5.0 s in physical time and its practicality on large-scale industrial reactors is not feasible. Hence, this method does not prove to be computationally viable for realistic models which contain far more fuel particles and require simulations over a longer period to allow for the achievement of possible steady state conditions and the statistical convergence of averaged results.

The combustion and gasification processes have been considered for a number of decades. An early comprehensive mathematical model was produced starting with simplified chemical reactions to determine emission predictions.²³ The first model to be regarded as a fully complete model considered fluidization modeling (FM) which models the emulsion phase and the bubbles through to the mass balance of the drying and devolatilization processes.²⁴ Unfortunately, FMs so far do not consider the fully complex gas-particle dynamics that CFD considers; however, they still maintain the multiphase flow dynamics with the inclusion of semiempirical fluid-dynamic correlations for the flow behavior in the bed. This model considered the drying and devolatilization processes to occur noninstantaneously, whereas Chejne et al.²⁵ considered these processes as instantaneous since drying and devolatilization take place very quickly in fluidized beds.

A number of devolatilization models have been implemented previously including the constant model,^{26,27} single rate model,²⁸ and the Kobayashi model.^{29,30} The most basic devolatilization model assumes the release of volatiles to occur at a constant rate²⁶ where the rate was later suggested to be 12/s.²⁷ The single rate model²⁸ assumes the rate of the volatile release is first-order dependent based on the amount of volatiles remaining in the coal. Unfortunately these models rely on data which would be specific to different coals; therefore, the general utility of the models would be limited to the available data extracted from the coals.

Received: November 18, 2010

Accepted: March 30, 2011

Revised: March 10, 2011

Published: April 11, 2011

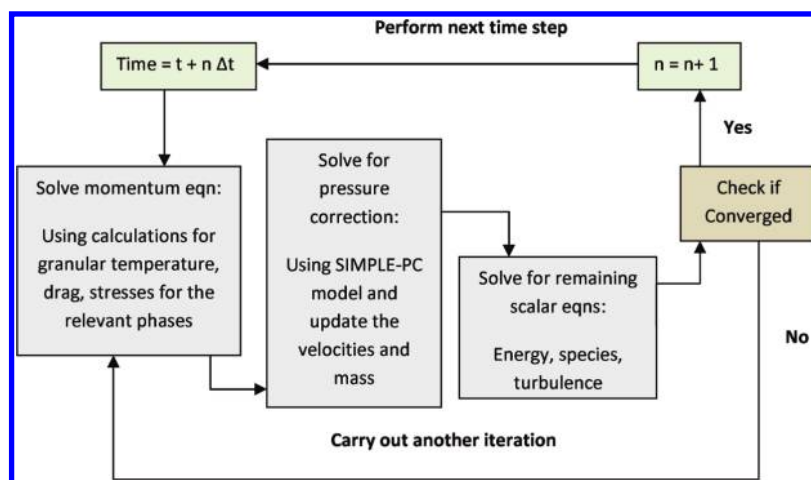


Figure 1. Solution procedure carried out in the present work.

Recently Eulerian-Eulerian modeling has been considered where Yu et al.³¹ carried out a two-dimensional Eulerian-Eulerian model of the gasification of Colombian coal based on experimental data from the literature.³² Their model included the pyrolysis, heterogeneous reactions, and homogeneous reactions and produced reasonable results for a sand bed. Their work was further extended to three-dimensions, also obtaining reasonable results.³³ However, their model considered a single solid phase for the coal and sand which is computationally more efficient but unrealistic. Our previous work considered a separate phase for the solid phases.³⁴ Our findings highlighted that the use of multiple phases better represents the bed behavior due to its ability to segregate phases of different material properties. Our previous work was also extended to incorporate limestone into the bed material which was the actual bed material used in the experimental data allowing for improved bed dynamics and the inclusion of limestone calcination. Unfortunately, the previous models only consider the effects of basic parameter variation, i.e., gas inlet velocities and reactor temperatures. There are a number of issues that can effect the gasification process including the amount of char available to instigate heterogeneous reactions, the inclusion of heat transfer coefficients, and bed height. Furthermore, previous results suggest that the steady gaseous compositions are achieved as early as 10.0–20.0 s;³⁴ therefore, extended simulations times need to be performed to confirm this assumption.

Limestone calcination was introduced to fluidization modeling (FM) by deSouza-Santos²⁴ and also adopted by Chejne et al.²⁵ Our previous work introduced limestone calcination to Eulerian-Eulerian CFD modeling highlighting that with a small residence time of 100.0 s slight changes in the gaseous composition were observed for a bed of char and limestone with a 50:50 ratio.³⁴ However the residence time needed to be increased significantly in order to observe an almost complete conversion as found by Wang et al.³⁵ who investigated the effects of temperature and residence time on the decomposition of limestone of similar sized particles in a CO₂ atmosphere and found that with a BFB temperature of 1193.15 K, the residence time for over 73% conversion of CaCO₃ to CaO was approximately 70 min.

The present work expands on our previous work³⁴ using an Eulerian two-fluid model for multiple phases to determine the effects of different parameter variations in the setup and models. User-defined functions (UDFs) are developed for two devolatilization models, while the initial conditions are varied in temperature, heat transfer coefficients, bed height, and bed material.

The simulated results of the base model are compared to results given in the literature first and further to the different model setups. Finally, limestone calcination is further expanded from our previous work to determine the effects of different bed ratios and over a longer period of time. This study is the first extensive parametric study to be carried out for an Eulerian-Eulerian coal gasification model.

MODEL SETUP

The Eulerian-granular model in ANSYS 12.0 was used to model the interactions between three phases: one gaseous phase and two granular particle phases within a fluidized bed taken from the literature.³² This model was chosen over the Eulerian-Lagrangian models as it is computationally more efficient with regards to time and memory. The model allows for the presence of the different phases in one control volume of the grid by introducing the volume fraction variable. The solid phases, one for limestone and the other for coal, both contain spherical granular particles of the same diameter. The phases are solved individually using the mass and momentum equations. The kinetic fluctuations between particles are considered using the kinetic theory of granular flow. The virtual mass and lift effects are negligible as the lift only affects particles of large diameters and this is not the present case. A complete description of the mathematical models that are utilized in the present work are given previously.³⁴

The solution procedure is given in Figure 1. The properties of the fluid, i.e., densities etc., are initially patch to the system. The momentum equation is solved using the properties available to calculate the relevant closure equations, i.e., drag, granular temperature, stresses. The values are then used to calculate the pressure correction equation³⁶ such that the continuity equation is satisfied and updates the velocities and mass. The remaining scalar equations, i.e., energy, turbulence, and species equations, are then solved. If it has not converged an additional iteration is performed, whereas if it has then the fluid properties are updated with those obtained and the cycle can begin again with the next time step. The commercial software ANSYS 12.0 was used to solve the governing equations. The discretization of the convective terms was carried out with the second-order upwind scheme. A time step of 1×10^{-4} was used to ensure quick convergence with a maximum of 100 iterations per time step.

Table 1. Heterogeneous, Homogeneous, and Calcination Reactions with Their Kinetic Rate Constants

heterogeneous reactions	kinetic rate constants	reaction
$C + O_2 \rightarrow CO_2$	$K_{Arr_1} = 1.04 \times 10^5 T_c \exp((-11200)/(T_c))$	R1
$C + H_2O \rightarrow CO + H_2$	$K_{Arr_2} = 342 T_c \exp((-15600)/(T_c))$	R2
$C + CO_2 \rightarrow 2CO$	$K_{Arr_3} = 342 T_c \exp((-15600)/(T_c))$	R3
$C + 2H_2 \rightarrow CH_4$	$K_{Arr_4} = 3.42 \times 10^{-3} \exp((-15600)/(T_c))$	R4
homogeneous reactions	kinetic rate constants	reaction
$CO + 0.5O_2 \rightarrow CO_2$	$K_1 = 1.0 \times 10^{15} \exp((-16000)/(T_g)) C_{CO} C_{O_2}^{0.5} \rho_g^{1.5}$	R5
$H_2 + 0.5O_2 \rightarrow H_2O$	$K_2 = 5.159 \times 10^{15} \exp((-3430)/(T_g)) T^{-1.5} C_{H_2}^{1.5} C_{O_2} \rho_g^{2.5}$	R6
$CH_4 + 2O_2 \rightarrow 2H_2O + CO_2$	$K_3 = 3.552 \times 10^{14} \exp((-15700)/(T_g)) T^{-1} C_{CH_4} C_{O_2} \rho_g^2$	R7
$CO + H_2O \rightleftharpoons H_2 + CO_2$	$K_4 = 2780 \exp((-1510)/(T_g)) [C_{CO} C_{H_2O} - (C_{CO_2} C_{H_2}) / (0.0265 \exp(3968/T_g))]$	R8
limestone calcination	kinetic rate constants	reaction
$CaCO_3 \rightarrow CaO + CO_2$	$K_{cal} = (3.07 \times 10^{11}) / (3.336 \times 10^7 p \exp(-20269/T_i)) \exp((-24670)/(T_i))$	R9

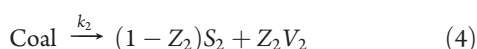
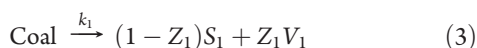
Although the model is the same as that carried out previously,³⁴ an additional devolatilization model is considered in the present model. A single rate model²⁸ assumes the rate of the volatile release is first-order dependent based on the amount of volatiles remaining in the coal. The kinetic rate of volatile release is given as



$$k = A \exp\left(\frac{-E}{RT_p}\right) \quad (2)$$

where $A = 4.92 \times 10^5 \text{ s}^{-1}$ and $E = 7.4 \times 10^7 \text{ J/kgmol}$.

The Kobayashi two-equation method³⁰ instantaneously handles the devolatilization of coal and volatiles release was carried out in our previous work.



$$k_i = A_i \exp\left(\frac{-E_i}{RT_p}\right) \quad (5)$$

S_i represents the char that is unreacted, V_i is the volatile produced, and the yield factors are given by Z_i . Kobayashi et al.³⁰ recommends that Z_1 be set to the fraction of volatiles determined by the proximate analysis as it represents devolatilization at lower temperatures. Z_2 should be set close to unity as it is the yield of volatiles at high temperatures. The rate constants k_1 and k_2 are given in Arrhenius form where $A_1 = 2 \times 10^5 \text{ s}^{-1}$, $A_2 = 1.3 \times 10^7 \text{ s}^{-1}$, $E_1 = 1.046 \times 10^8 \text{ J/kgmol}$, $E_2 = 1.67 \times 10^8 \text{ J/kgmol}$, $Z_1 = 0.418$, and $Z_2 = 1.0$.

An overview of the heterogeneous and homogeneous reactions that take place in the present work are given in Table 1.

Initial and Boundary Conditions. The present work was set up according to the experimental study of Colombian coal by Ocampo et al.³² and is an extension of our previous work.³⁴ Using the Eulerian-Eulerian model, the solid phases made up an initial bed of limestone and char that was set to the height of 1.0 m with a volume fraction of 0.48; an equal volume fraction was used for the two solid phases of 0.24 each. The solids properties, operating conditions, and experimental results are given in Table 2. For the two-dimensional results, a base case is carried out using model 1 in

Table 2. Characteristics of Solids

coal properties			
<i>proximate analysis (wt%)</i>			
moisture			2.6
volatile matter			41.8
fixed carbon			54.1
ash			1.5
<i>ultimate analysis (wt%)</i>			
carbon			75.3
hydrogen			5.4
oxygen			15.6
nitrogen			1.8
sulfur			0.4
ash			1.5
<i>others</i>	<i>limestone</i>	<i>coal</i>	<i>char</i>
mean particle size (mm)	0.60	0.62	0.60
apparent density (kg/m ³)	2700	1250	450
high heating value (kJ/kg)		29695	

Table 2. The other models will be considered for the three-dimensional simulations. Figure 2 displays a sketch of the model setup used.

A two-dimensional mesh was created using 2215 quadrilateral cells. The cell size in the horizontal direction was 0.01 m, while the vertical direction was set to 0.02 m creating a domain of (22×100) cells as used previously.^{31,37} The region near the coal inlet was further reduced to a minimum of 0.0004 m horizontally and 0.0008 m vertically to correctly capture the devolatilization characteristics near the fuel inlet. The cells near the wall were not refined further as the purpose of the model was to capture the gasification processes within the bed and not the near wall behavior.

The three-dimensional simulations will be carried out using a mesh of 66243 cells. The cell size in the horizontal direction was taken to be 0.02 m, while the vertical direction was set to 0.02 m. Similarly, the three-dimensional mesh refines the region near the coal inlet further to a minimum of 0.0004 m horizontally and 0.0008 m vertically to correctly capture the devolatilization characteristics near the fuel inlet as the fuel is introduced.

Boundary conditions for the gas phase were set to no-slip, and for the particulate phase a tangential slip condition was imposed.³⁸

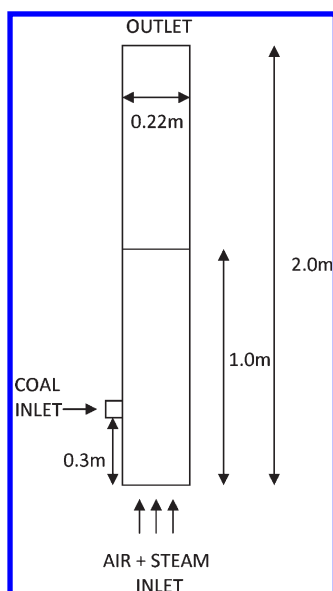


Figure 2. Experimental setup of the reactor.

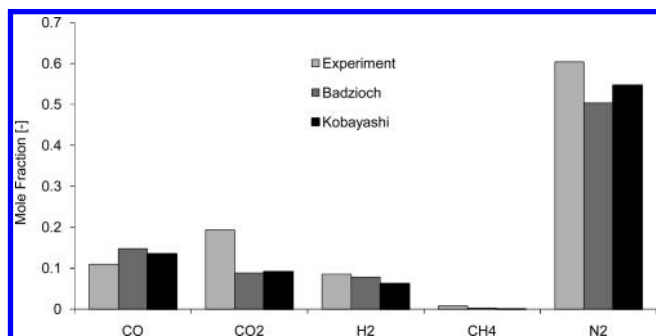


Figure 3. Mole fraction comparison of the gaseous products from the Badzioch and Kobayashi models with experimental data from Ocampo et al.³²

RESULTS

Devolatilization Modeling. Two devolatilization models were tested, and the mole fractions of their gaseous products are compared with experimental data in Figure 3. Both models agree fairly well with the experimental data although there is a distinct variation in the mole fraction of CO₂. The low concentration of CO₂ compared to that observed from the experimental data was determined previously³⁴ as a result of bed material composition where the experimental bed consisted primarily of limestone, whereas this model is formed of both char and limestone in a 50:50 ratio. As a result, the char consumed CO₂ faster via the Boudouard reaction (R3) subsequently leading to a significant increase in CO. This also agrees with the findings of Gerber et al.³⁹ who carried out a simulation of a biomass BFBG with a char bed. The concentrations of CH₄ in Figure 3 are extremely low and not clear; therefore, Figure 4 focuses on the CH₄ compositions. Both models underpredict the mole fraction of CH₄ which could be down to the low mass fraction of CH₄ given by the Loison and Chauvin correlation⁴⁰ for the yield of volatiles released during devolatilization; therefore, a study of the various yield correlations would be advantageous. However, this would not produce an increase in CH₄ using the Badzioch model compared to the Kobayashi model suggesting the different

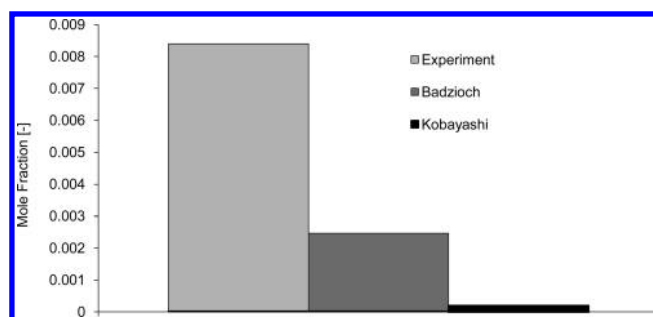


Figure 4. The mole fraction comparison of methane, CH₄, from the two devolatilization models with the experimental data from Ocampo et al.³²

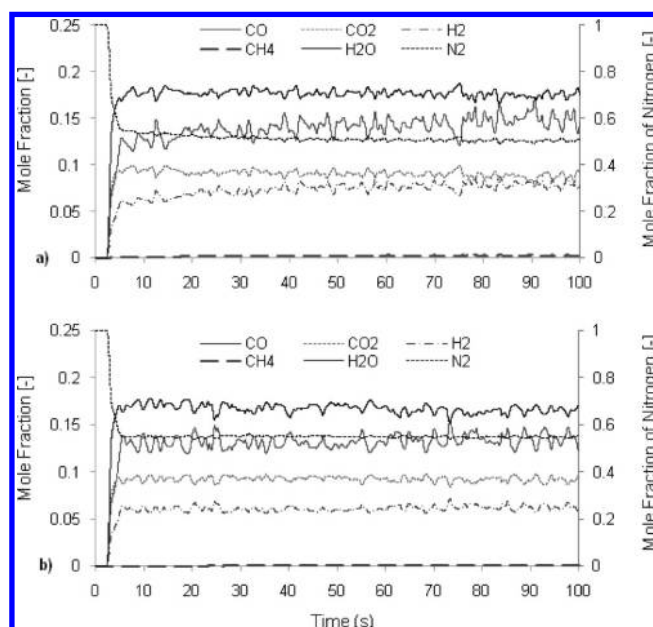


Figure 5. The instantaneous mole fraction of the gaseous products over a 100.0 s period through the outlet for the a) Badzioch and b) Kobayashi devolatilization model.

modeling assumptions of the devolatilization models would lead to this.

Figure 5 displays the instantaneous mole fraction of the gaseous products over a 100.0 s period, through the outlet, for both devolatilization models. It can be seen that the Kobayashi devolatilization model appears to have reached steady state conditions for all gaseous species, whereas the Badzioch model does not. The species CO and H₂ increase in mole fraction with time, whereas CO₂ and H₂O decrease slightly. This could be due to the Kobayashi model's incorporation of yield factors which modify the volatile release based on local temperature, whereas the Badzioch model does not account for this. Since particles can migrate due to the mixing behavior of the bed the local temperature would change. The Kobayashi model would recognize this change in temperature and choose its volatile release accordingly, whereas the Badzioch model would assume the same volatile release for lower temperatures as for higher temperatures. The increased concentration of these volatile species in regions of lower temperatures would promote more heterogeneous reactions leading to a slight increase in their products, namely CO and H₂ as observed in Figure 3.

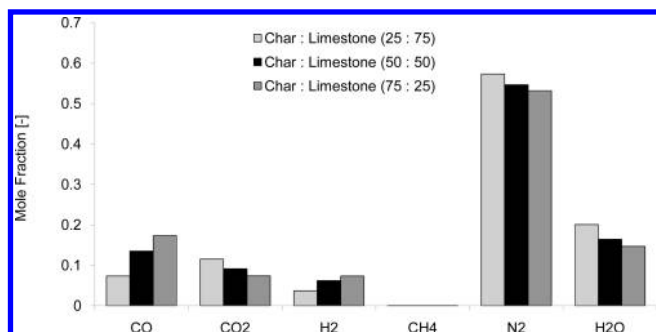


Figure 6. Average mole fraction of the gaseous products through the outlet for varying bed compositions.

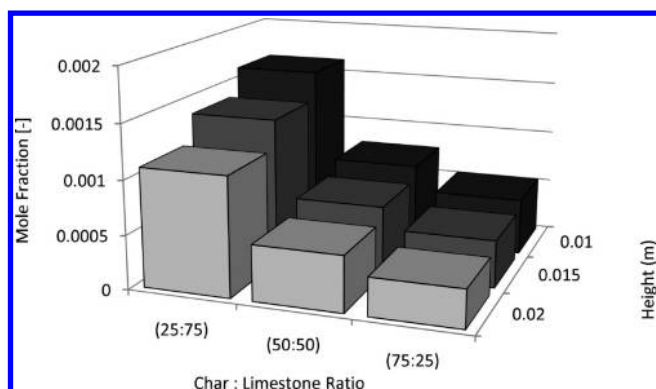


Figure 7. Average mole fraction of O₂ at different heights near the air inlet for the three bed compositions.

The increase in H₂ would explain why the concentration of CH₄ in Figure 4 is higher for the Badzioch model compared to the Kobayashi model. A higher concentration of H₂ would influence the methanation heterogeneous reaction resulting in an increase in CH₄. It would be beneficial to allow the Badzioch model to continue running for a longer period to allow for steady state conditions to be achieved. Since the Badzioch devolatilization model does not appear to have reached steady state conditions after 100.0 s with regards to mole fraction composition, the Kobayashi model was carried out for the remaining parametric models.

Bed Material. As discussed in the previous section, the composition of char and limestone can greatly influence the concentration of the gaseous products. Additional models were carried out modifying the base case which had a bed with a 50:50 ratio (char:limestone) to a limestone dominating bed (25:75) and char dominating bed (75:25). The mole fraction of the gaseous products are given in Figure 6. It is clear that increasing the percentage of char in the bed results in an increase in CO and decrease in CO₂. This is due to a higher presence of char promoting the combustion reaction leading to more CO₂ being produced. The CO₂ is consumed by the Boudouard reaction (R3) to produce more CO. Increasing the amount of char would increase the instances of all heterogeneous reactions taking place, including further up the bed where the steam gasification reaction (R2) produces further CO and H₂. This is also observed in Figure 6 where there is an increase in the concentration of H₂ with increasing char content.

Figure 7 shows the average mole fraction of O₂ at different heights near the air inlet for the three bed ratios of char:limestone, namely 25:75, 50:50, and 75:25. It can be seen that the bed with the 25:75 ratio model has a higher mole fraction of O₂ at all three

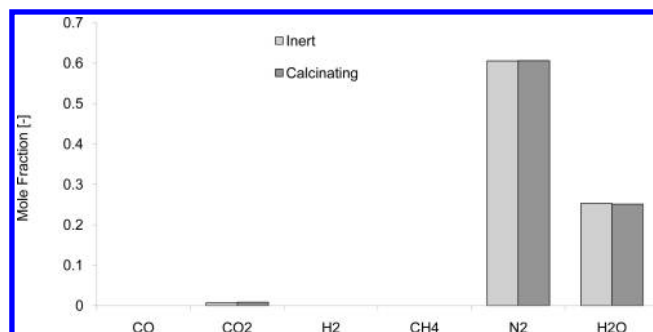


Figure 8. Average mole fraction of the gaseous products with a bed containing only inert limestone or calcinating limestone.

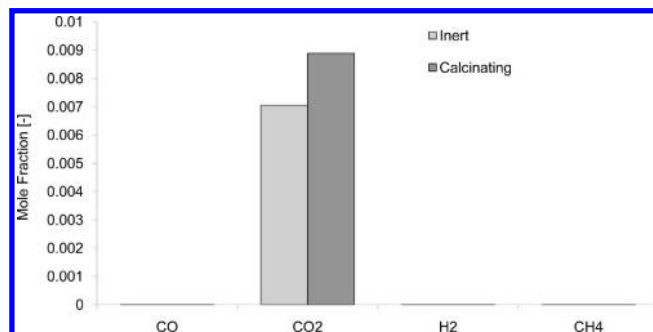


Figure 9. Close up of the gaseous composition of the products for a bed of inert and calcinating limestone.

heights 0.01 m, 0.015 m, and 0.02 m. The average mole fraction decreases with increasing char quantity as more char is available to participate in heterogeneous combustion. Since a lower char to limestone ratio has a higher O₂ concentration further up the bed, oxidation reactions can take place more over a great area leading to an increase in CO₂ and H₂O as can be seen in Figure 6.

It is worth highlighting that the limestone calcination model was carried out in all instances; therefore, an assumption could be made that increasing the amount of limestone would result in an increase in CO₂ due to its release during the calcination process. However, we showed previously³⁴ that after 100.0 s the calcination process only released a small amount of CO₂. This agreed with the findings of Wang et al.³⁵ who found that for similar conditions it took approximately 70 min for roughly 73% conversion of limestone into CO₂ and CaO. To further highlight the effects of limestone calcination a bed consisting of 100% limestone was modeled with inert limestone and calcinating limestone. The results given in Figure 8 show a completely different composition compared to that given with char present. This is due to the heterogeneous reactions only taking place with the limited char produced by the devolatilization process. A closeup of the products, CO, CO₂, H₂, and CH₄, in Figure 9 shows a significant increase in the concentration of CO₂ due to limestone calcination; however, as expected this increase is only slight in comparison to the influence heterogeneous reactions have on the gaseous compositions.

The low concentrations on CO, H₂, and CH₄ are due to the homogeneous reactions taking place throughout the bed as opposed to beds containing char where the reactions are limited to O₂ enriched near-inlet region. Since there is very little char in the bed O₂ does not get consumed; therefore, the volatile products released near the fuel inlet are consumed via the oxidation homogeneous reactions producing CO₂ and H₂O (Figure 8).

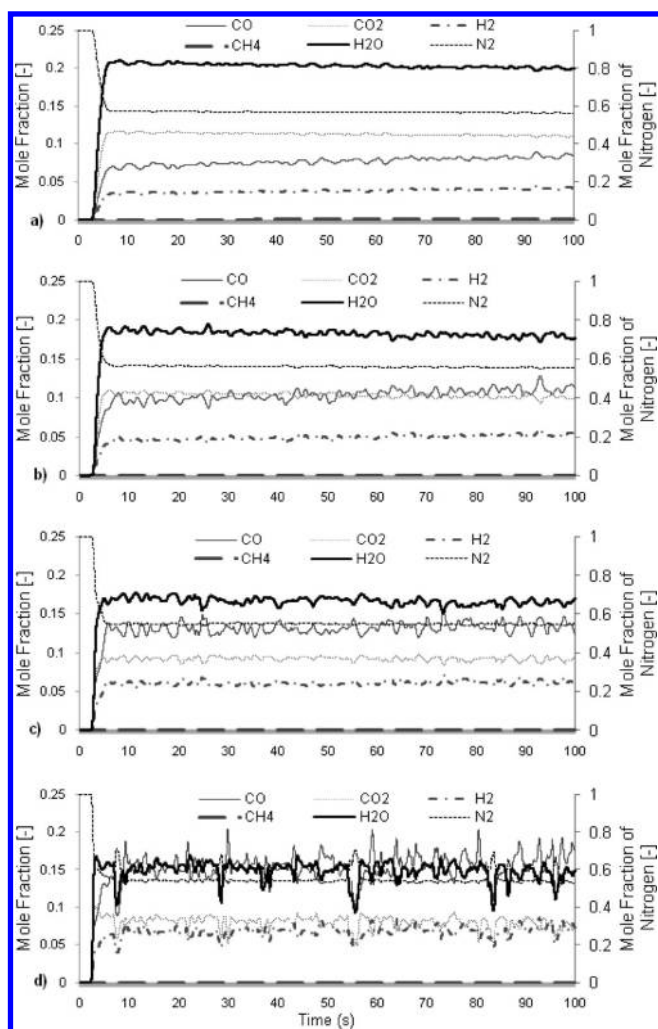


Figure 10. The instantaneous average mole fraction of the gaseous species over a 100.0 s period for bed heights: a) 50 cm, b) 75 cm, c) 100 cm, and d) 125 cm.

Bed Height Variation. Our previous work³⁴ showed that the water-gas shift had not reached equilibrium for a bed height of 100 cm, so in the present study simulations were carried out with various bed heights. The results given in Figure 10 show the instantaneous mole fraction of the gaseous species over a 100.0 s period for bed heights of 50 cm, 75 cm, 100 cm, and 125 cm. The increased magnitude of the fluctuations with increasing bed height indicate that the water-gas shift has not had sufficient time to reach equilibrium before exiting the reactor. It is commonly acknowledged that it is highly unlikely for water-gas shift reaction to reach equilibrium within lab scale reactors due to the reduced area of freeboard space. A bed height of 50 cm in Figure 10a) shows a significant reduction in the fluctuation of the gaseous species upon exit. This lower bed height increases the area of the freeboard providing more space for the relevant species, namely CO, CO₂, H₂, and H₂O, to compete in the water-gas shift reaction thus indicating that equilibrium can be obtained in a small scale reactor providing the freeboard is sufficiently tall enough. The bed height of 125 cm shows very strong fluctuations since the average mole fraction results are taken at 200 cm leaving limited space for the species to adapt through the water-gas shift reaction.

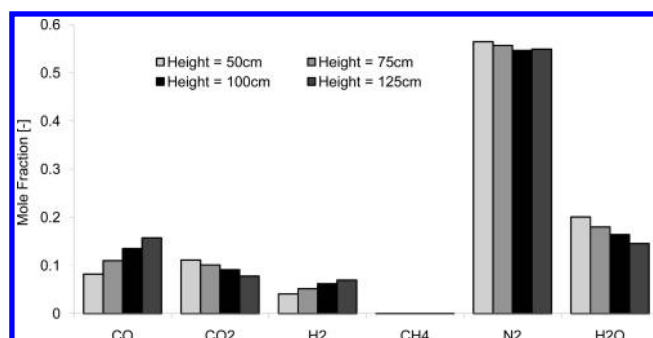


Figure 11. The average mole fraction of each gaseous product through the outlet over a period of 100.0 s for varying bed heights.

From as early as 5.0 s the composition of the species through the outlet remains relatively steady with the fluctuations varying depending on bed height. The mole fractions of N₂ and CH₄ appear more consistent with average mole fractions of approximately 55% and 0.02%, respectively, although CH₄ is so low that it is not as apparent in the graph. This is due to their nonparticipation in any of the reactions except for the methanation reaction where the reaction rate is small and would not influence greatly the variation in CH₄ fluctuations.

It can be seen however that lower bed heights, 50 and 75 cm, display a gradual increase in CO and H₂ species over time indicating that for such a small bed height the compositions do not reach a steady state conditions compared to higher bed heights. This may be due to smaller bed heights containing less char; therefore, CO₂ and H₂O would not be consumed as effectively through heterogeneous reactions. Such high concentrations of CO₂ and H₂O would affect the water-gas shift reaction leading to the gradual increase in their opposing species H₂ and CO. The mole fractions of CO₂ and H₂ in Figure 11 decrease with increasing bed height as more increasing char levels lead to more exposure of gases to heterogeneous reactions, while products of such reactions, CO and H₂, increase with increasing bed height.

Bed Temperature Variation. Our previous work,³⁴ highlighted how the local temperatures within the bed depend on which dominating reactions that are taking place locally. This was seen to be due to the different reactions producing or consuming heat depending on whether they are exothermic or endothermic, respectively. Reactions are also highly temperature dependent; therefore, the effect of bed temperature on the composition of the exhaust gases is studied with models using temperatures lower (1078.15 K) and higher (1178.15 K) than the base case (1128.15 K). The average mole fraction of the gaseous species are given in Figure 12. Results show that bed temperature is an important influence on the gasification processes. Increasing the temperature results in an increase in CO and H₂ species and a decrease in CO₂ and H₂O. This is due to the highly temperature dependent heterogeneous reactions. As the temperature increases the reactions take place faster leading to a faster consumption of the reactants H₂O and CO₂ through the steam gasification reaction and Boudouard reaction, respectively. This subsequently leads to an increase in their products CO and H₂, which is apparent in Figure 12.

Figure 13 displays the instantaneous mole fraction of gaseous species through the outlet over a 100.0 s period. The fluctuations of the four water-gas shift species increased in magnitude as the bed temperature increased. For the 1178.15 K bed the fluctuations were highly erratic possibly due to the levels of CO and

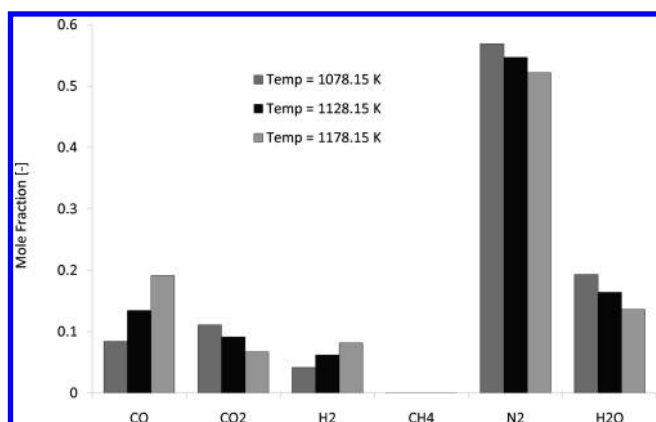


Figure 12. The average mole fraction of each gaseous product through the outlet over a period of 100.0 s for varying temperatures.

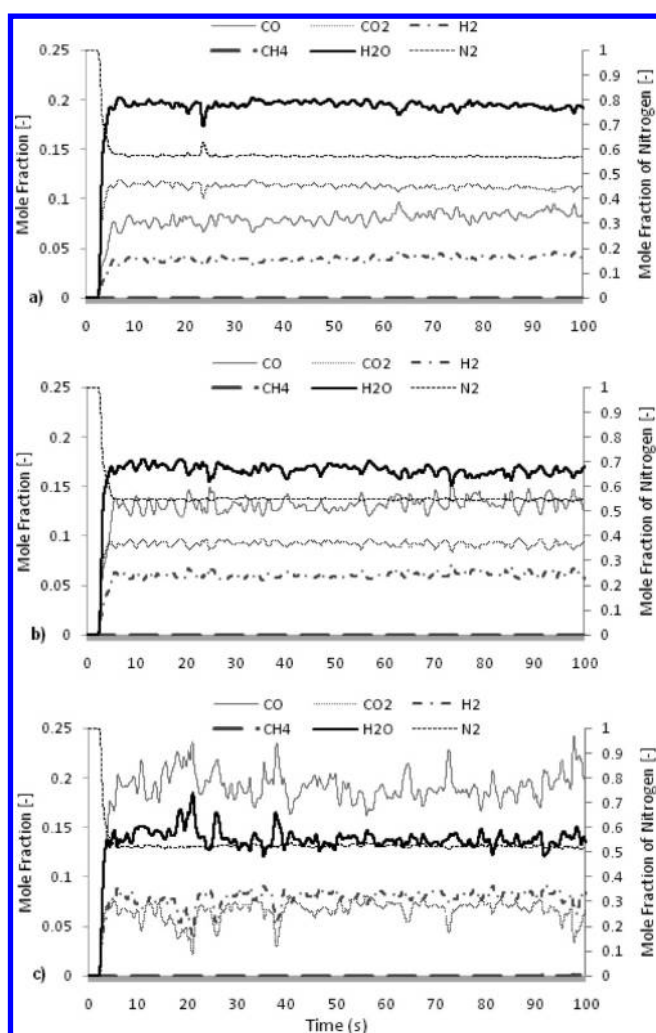


Figure 13. The instantaneous mole fraction of gaseous species through the outlet over a 100.0 s period for bed temperatures a) 1078.15 K, b) 1128.15 K, and c) 1178.15 K.

H₂O being the dominating species. These species react together as the forward reactants of the water-gas shift reaction; therefore, their dominance within the freeboard compared to the lower levels of the competing backward reactants would not allow for

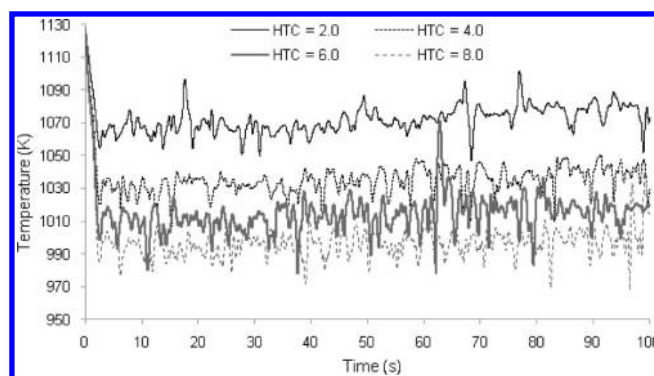


Figure 14. The instantaneous average temperature through the outlet over a period of 100.0 s for varying heat transfer coefficients (W/m² K).

equilibrium to be achieved easily, especially in such a small freeboard area. Therefore, it can be assumed from Figure 10 and Figure 13 that should the two dominating species in the freeboard be the reactants on the same side of the water-gas shift reaction, e.g., CO and H₂O being the reactants for the forward reaction, then the attainability of equilibrium would be very difficult. Having dominating species on both sides of the reversible reaction displays smaller fluctuations in the instantaneous mole fractions indicating an improved chance of reaching equilibrium state.

The water-gas shift reaction is dependent on concentration as well as temperature; therefore, as the concentration of the forward reactants peaks the reaction takes place faster. This increases the concentration of their products, CO₂ and H₂, while causing a sharp decrease in CO and H₂O due to their conversion. The continual supply of increased forward shift reactants by heterogeneous reactions and as products of the backward shift reaction then leads to a peak in their mole fractions again starting the cycle once more. Occasionally, there appears to be a dramatic peak in CO and H₂O, for example at approx. 38.0 and 72.0 s in Figure 13 (c). This could also be due to slight numerical instabilities that can occasionally occur, particularly near the exit of the reactor where backflow could take place.

Heat Transfer Coefficients. The model was adjusted to incorporate heat transfer at the walls with four different heat transfer coefficients, 2, 4, 6, and 8 W/m² K. Since there were no actual experimental data providing information on relevant heat transfer coefficients for this setup, the values were chosen to make similar comparisons with the results observed by Gerber et al.³⁹ for a biomass gasifier. The inclusion of heat transfer coefficients have a strong impact on the average gaseous temperature leaving the reactor as seen in Figure 14. Higher temperatures are observed with decreasing heat transfer coefficients as the heat loss through the walls is reduced. This was previously observed by Gerber et al.³⁹ who also found, as seen in Figure 14, that lower heat transfer coefficients did not reach steady state conditions while higher ones did.

We observed the influence that temperature had on the gasification and homogeneous reaction rates in section Figure 11. However it can be seen in Figure 15 that although the variation of heat transfer coefficient greatly affects the exiting gaseous temperature it does not affect the composition of the exiting gases. The average mole fraction of the gaseous products for the four different heat transfer coefficients does not show a great deal of variation. This is due to the heat transfer coefficients only

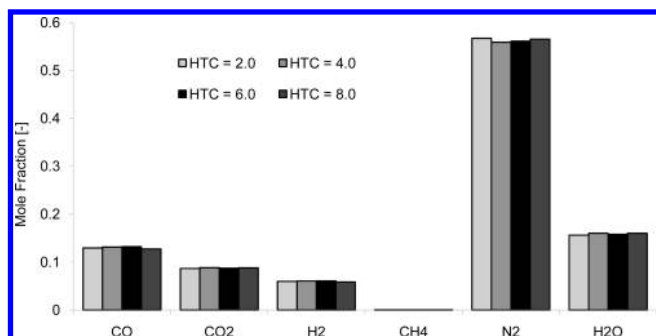


Figure 15. The average mole fraction of the exiting gaseous products for the four different heat transfer coefficients ($\text{W}/\text{m}^2 \text{K}$).

Table 3. Operating Conditions and Experimental Results

operating conditions	model 1	model 2	model 3	model 4
air supply (kg/h)	21.9	17.0	19.4	21.9
steam supply (kg/h)	4.7	4.7	4.7	4.7
coal feed (kg/h)	8.0	8.0	8.0	8.0
limestone feed (kg/h)	0.8	0.8	0.8	0.8
air and steam				
temp at entrance (K)	693.15	686.15	695.15	708.15
temperature of reactor (K)	1128.15	1085.15	1114.15	1139.15
experimental results	model 1	model 2	model 3	model 4
H ₂ (%)	8.53	8.84	9.36	7.88
CO ₂ (%)	19.31	18.38	14.40	15.60
N ₂ (%)	60.37	61.10	64.62	64.52
CH ₄ (%)	0.84	1.07	1.34	1.01
CO (%)	10.94	10.59	9.97	10.94

effecting the local wall regions and in the dense particulate bed this is neglected as the high bed temperature dominates. However, in the freeboard the temperatures from the wall are transported via convection through the gases therefore increasing the temperature in this region. The slight fluctuations observed in Figure 15 could be due to the variation in freeboard temperature which affects the reaction rate of the water-gas shift reaction. This would explain the larger difference being observed between the heat transfer coefficient of $2.0 \text{ W}/\text{m}^2 \text{K}$ and the other three coefficients as the temperature profile is significantly higher than the remaining coefficients in Figure 14.

Extended Simulation Times. The instantaneous gaseous compositions appear to be steady from as early as 10.0–20.0 s, and previous assumptions in the literature^{39,34} have suggested that the gaseous compositions reach steady state by 100.0 s. However it is worth extending the simulation times further to confirm this assumption. Unfortunately, due to the extensive times required to carry out these reaction models a grid dependency check is performed to determine appropriate cell sizes and time steps which would carry out the simulations in a faster time without too much loss of accuracy.

Table 4 displays twelve separate cases consisting of three grid sizes; a refined grid $-0.01 \text{ m} \times 0.01 \text{ m}$, the base case grid $-0.01 \text{ m} \times 0.02 \text{ m}$, and a coarse grid $-0.02 \text{ m} \times 0.02 \text{ m}$; that were modeled using four different time steps: 0.00005 s, 0.0001 s, 0.0005 s, and 0.001 s. The cases ran for 20.0 s using the model setup of model 1, given in Table 3. For reference, the initial base case carried out throughout this work, which was also applied previously for a different model in the literature,^{31,37} is given as case 6 in Table 4.

Figure 16 displays the performance of the different cases showing the time taken in hours to run to 20.0 s along with the number of cells involved in the calculations using 8 processors. As

Table 4. Grid Dependency Carried out with Different Cell Sizes and Time Steps

case	cell size horizontal (m) \times vertical (m)	time step (s)
1	0.01×0.01	0.00005
2	0.01×0.01	0.0001
3	0.01×0.01	0.0005
4	0.01×0.01	0.001
5	0.01×0.02	0.00005
6	0.01×0.02	0.0001
7	0.01×0.02	0.0005
8	0.01×0.02	0.001
9	0.02×0.02	0.00005
10	0.02×0.02	0.0001
11	0.02×0.02	0.0005
12	0.02×0.02	0.001

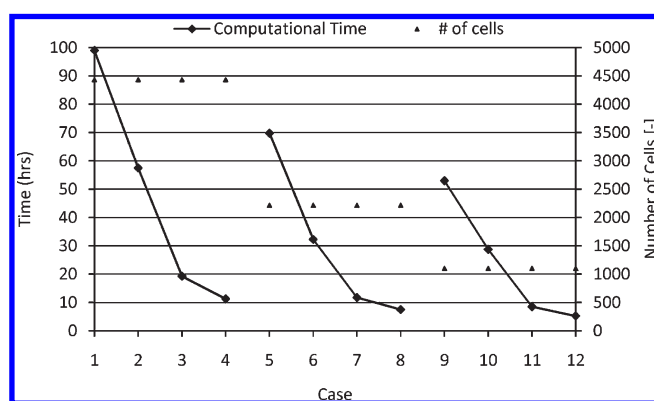


Figure 16. Performance of the different grid dependency cases which ran for 20.0 s.

expected, as the grid becomes coarser the number of cells reduces and the time taken to run the simulations to 20.0 s reduces. The variation in time step impacts the duration of the run times greatly as smaller time steps require more time steps within the same period of 20.0 s to complete. Increasing the time step reduces the number of time steps required to ensure convergence is achieved. This is observed by looking at the time difference between the models run with 0.0005 and 0.001 s time steps. The time duration display very little difference even though the number of time for the 0.001 s time steps required half the number of time steps within the 20.0 s period. Due to the large time steps the model requires more iterations before reaching convergence; therefore, time is not necessarily gained to benefit these large time steps.

The effect of different grid sizes can be seen in Figure 17 which compares the volume fraction of the gases at 20.0 s for the smallest time step models: case 1, case 5, and case 9. The smallest time step allows for very fast convergence; therefore, discrepancies seen would be due to grid size instead of a coarse time step. The finest grid, case 1, shows clear defined bubbles for both small and large bubbles with the interaction between the bubbles and dense particulate phase being refined and the bubbles containing higher gas volume fractions. The coarsest grid, case 9, however displays similar bubble structures except the bubbles appear larger as the interaction of the bubble with the bed appears thicker and also the bubbles appear to have lower volume fractions. This is again due

to the rough estimations made in local area, a smaller grid cell would detect a gas volume fraction of say 0.99 whereas a grid cell with twice the size would average this value with the surrounding values in the cell which could contain more particles thus reducing the value. The effects of coarser averaging is particularly seen at the base of the bed where there are small bubble formations due to the endogenous products of heterogeneous reactions. The refined bed captures these small bubble formations, whereas increasing the grid size reduces the ability to capture them as rougher estimations are made with regards to the local behavior within the vicinity.

The mesh used in case 5 contains a horizontal grid size which is the same as case 1 but the same vertical grid size as case 9. The formation of some smaller bubbles are captured at the lower

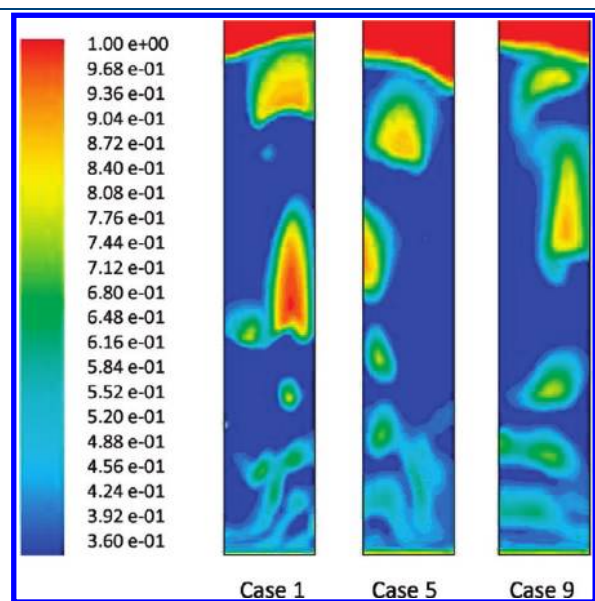


Figure 17. Gas volume fractions taken at 20.0 s for three different mesh sizes using the smallest time step: case 1, case 5, and case 9.

regions of the bed. The large bubble at the top of the bed shows refinement for the bubble interaction with the bed on the left and right side of the bubble; however, the top of this bubble and the base of the react show the effects of the coarser grid in the vertical direction as the results appear less refined. Different flow distributions are achieved at the same time by the three models. As coarser grids produce rougher estimations for the flow dynamics these less accurate values would then be used to calculate the results at the next time step. Continuation like this would subsequently lead to a different flow distribution in an already heterogeneously bubbling bed.

The corresponding gas velocity vectors are given in Figure 18 showing how much more refined the mesh in case 1 is compared to the mesh in case 9. Each node gives the velocity value and which is scaled according to the local velocity of the gases. Comparison with Figure 17 shows the gas traveling faster in the dilute regions, i.e., through the bubbles, as the gas travels the easiest route possible with the least resistance. Since bubbles contain a low concentration of particles, which act as obstacles, the gas prefers to travel via this route. Although the flow displays a different distribution for the three cases at 20.0 s, the gas velocities are very similar regardless of the grid size. A peak velocity is observed in case 1 within a bubble which is significantly faster compared to the velocities observed in the other two cases; however, this would be due to the volume fraction of the gases in this region being very dilute (in Figure 17). Furthermore, it could also just be specific to the flow distribution captured at this specific point in time.

While the flow dynamics display slight differences between the grid sizes, it is worth comparing the average gaseous compositions for all cases to determine the effects grid size has on the reaction kinetics. Figure 19 shows the exiting gaseous compositions which were average over a period of 10.0 s for each of the twelve cases. There appears to be very little variation in the average gaseous compositions across all the models probably because any differences in the gaseous composition produced are a result of averaging over coarser grids. These variations would be

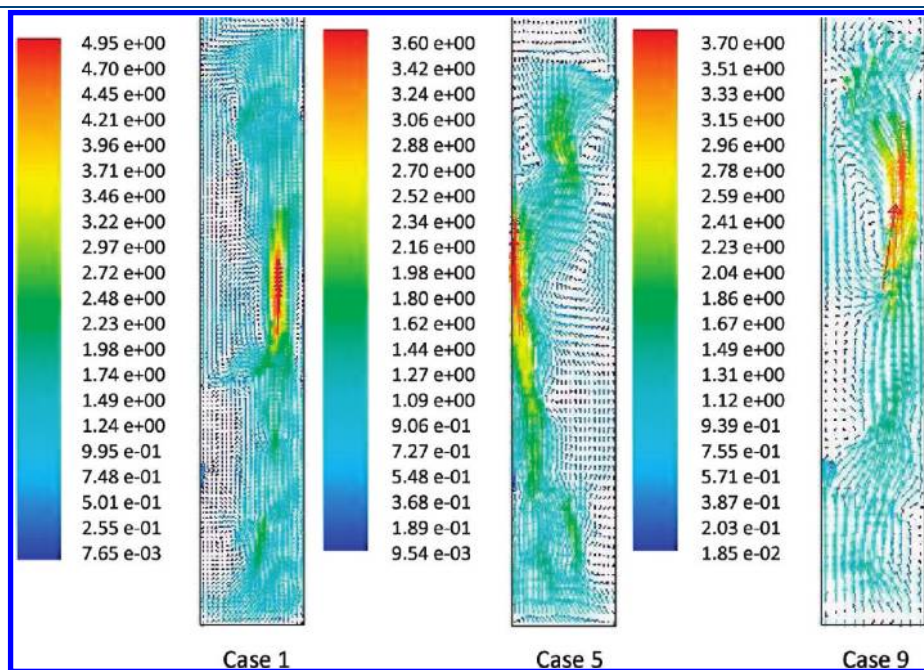


Figure 18. Gas velocity vectors taken at 20.0 s for three different mesh sizes using the smallest time step: case 1, case 5, and case 9.

slight and would be negligible by the time the gases reach the outlet because the water-gas shift reaction would adjust the compositions accordingly leading to similar compositions.

For the benefit of modeling the gaseous composition alone, a coarse grid would work just as effectively as a refined grid. The coarser grid of $0.02 \text{ m} \times 0.02 \text{ m}$ will be utilized in the extended simulation models as the gaseous compositions are the main focus of this study; however, the time step chosen will be 0.0005 s , i.e., case 11, allowing for a faster simulation time than the previously used case 6 without compromising too much accuracy by increasing the time step. A limestone dominated bed (char:limestone = 25:75) was chosen as

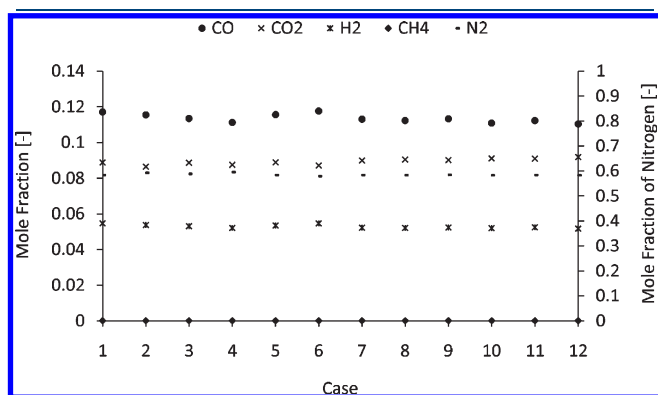


Figure 19. Mole fraction of exiting gases for the different models.

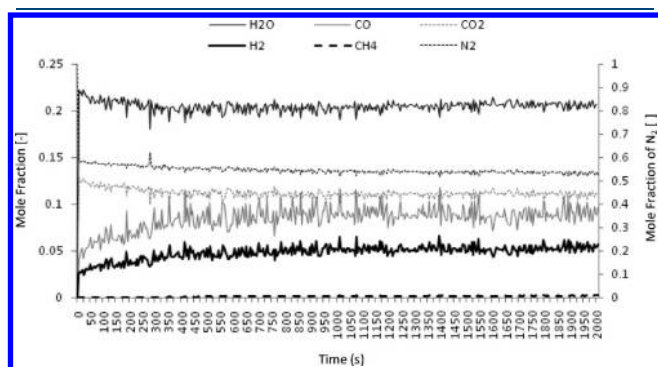


Figure 20. Instantaneous average gaseous composition over a period of 2000.0 s using case 11 from Table 4.

the results shown in the previous section, Figure 5 closely resembled the experimental results given in the literature.³² The extended model ran for 2000.0 s, and the instantaneous average mole fractions of the gases leaving the reactor are given in Figure 20.

The results in Figure 20 were obtained at 5.0 s intervals which explains the dramatic peaks that can be seen, especially in the water-gas shift species where the compositions are expected to vary as the reactants try to reach an equilibrium. It can be seen that the results reach steady state; however, this seems to occur after about 400.0 s suggesting that while the previous models which were carried out to 100.0 s may appear to have reached steady state due to the smaller time intervals, 0.005 s, at which the data were extracted which would suppress the increasing trend, they had not and in order to obtain sufficient time averaged composition results the simulation time needs to be extended further. The compositions were averaged for the last 50% of the 2000.0 s simulation and the 100.0 s simulation times, i.e., averaged between 1000.0 and 2000.0 s and 50.0–100.0 s, respectively. The results are compared to the experimental data given from Ocampo et al.³² in Figure 21.

The simulation that ran for 2000.0 s is averaged over a larger time period; therefore, the results would provide a better representation of the compositions over this extended time period, whereas the results from the 100.0 s are not only taken before steady state has been achieved but averaged over a shorter time period hence reducing the accuracy. The bar chart shows clear differences between the different simulations. The longer simulation shows an increase in the CO, H₂, and CH₄ due to the continual build up after the 100.0 s period of these products from the heterogeneous reactions. The CO₂ and H₂O, which gave an average mole fraction of 0.2113 for the 100.0 s simulation and 0.2049 for the 2000.0 s, reduces slightly which would be due to the water-gas shift being strongly influenced by the significant increase in CO and H₂. The results for N₂ throughout this work are given as the remaining composition once the other species had been accounted for.

Mass variations. The mass of the char and coal in the reactor for the first 1000.0 s of the limestone dominating bed and grid case 11 are given in Figure 22. As expected, the char shows a gradual decrease as the char gets consumed by heterogeneous reactions. Since the mass of the char depends on the consumption of the char through heterogeneous reactions as well as its production during the devolatilization process, the continual decrease in the char mass indicates the consumption takes place faster than the production. Therefore the reactor would eventually run out of char. The coal

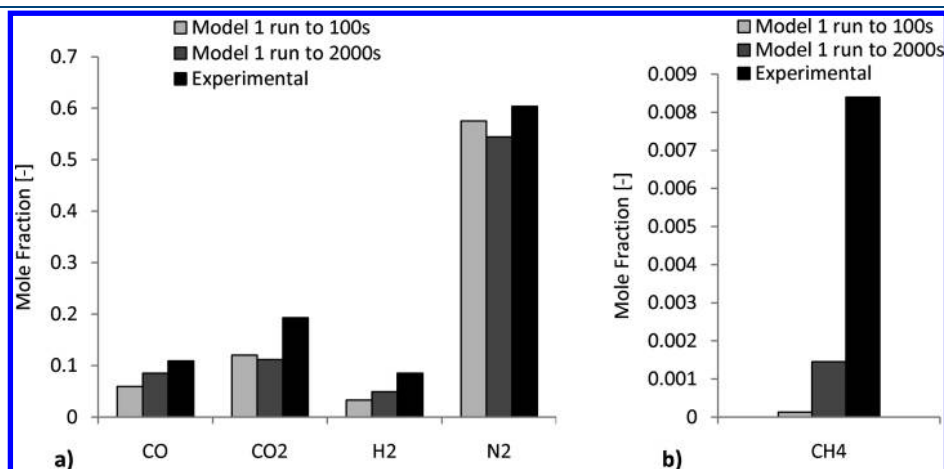


Figure 21. Average mole fraction of a) the dominant exiting gases and b) CH₄ after 100.0 and 2000.0 s of simulation time.

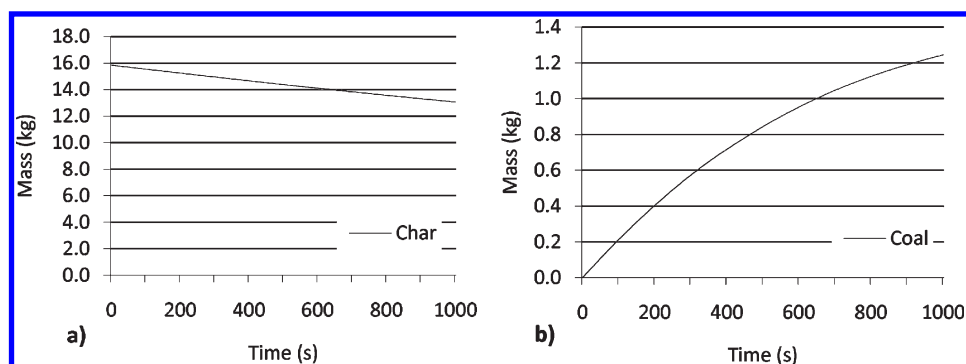


Figure 22. Mass of a) the char and b) the coal in the reactor during the first 1000.0 s of simulation time.

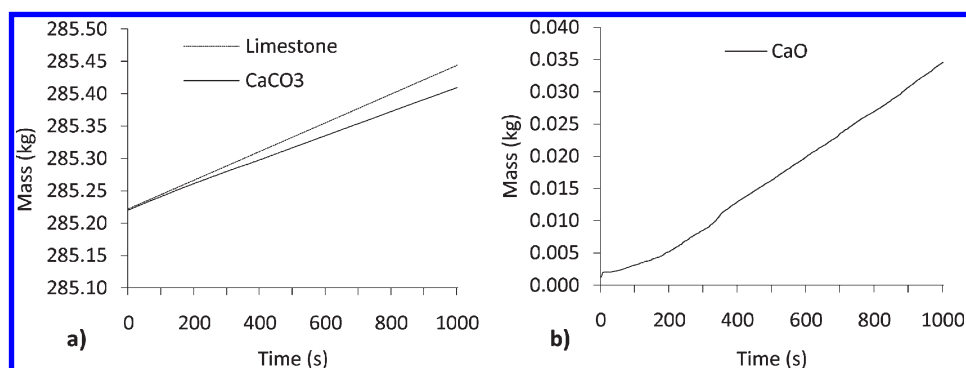


Figure 23. Mass of a) the complete limestone phase and the mass contribution from CaCO₃ and b) the contribution of CaO in the reactor during the first 1000.0 s of simulation time.

however increases quite fast at the beginning of the simulation and levels off gradually. This is due to the coal being introduced into the reactor at the beginning and building up. As coal degradation takes place the coal gradually breaks down into its constituents, namely volatiles and char, reducing the mass of coal leading to total mass leveling out as the reactor becomes accustomed to the introduction and degradation rates of the total coal in the bed.

The masses of the total limestone, CaCO₃, and CaO are provided in Figure 23 for the first 1000.0 s for the limestone dominating bed. The mass of the limestone phase shows a steady increase which is expected as the bed is continually being supplied limestone through the fuel inlet at a rate of 0.8 kg/h. The mass of CaCO₃ is the only component of the limestone at the beginning of the simulation before limestone calcination takes place. As the calcination reaction starts converting CaCO₃ into CaO and CO₂ there is a gradual decrease in the mass of CaCO₃ while the CaO gradually increases. The graph of the CaO mass shows a different behavior at the beginning of the simulation as the reactor attempts to reach steady state, but once steady state appears to be achieved at around 350.0–400.0 s the CaO increases at what appears to be a steady rate. This time period agrees well with the results shown previously in Figure 20 also displaying steady state behavior for the mole fraction of the exiting gases.

THREE-DIMENSIONAL MODELING

The three-dimensional model was set up as the two-dimensional model only without the inclusion of limestone calcination as the previous results displayed a minimal influence on the gas

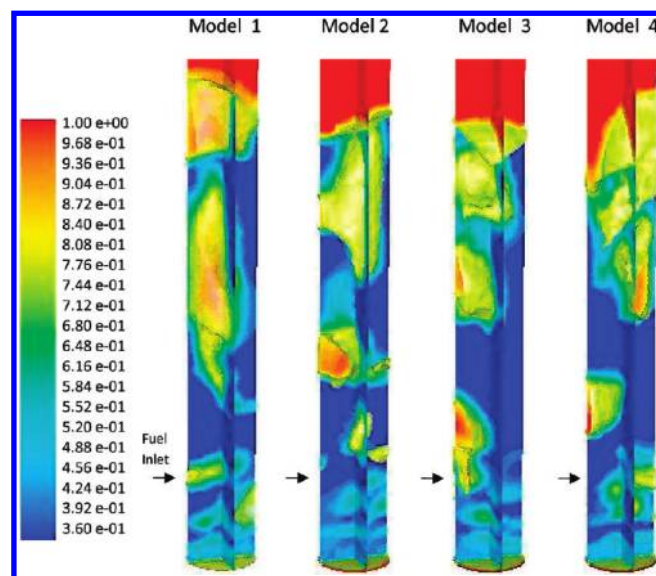


Figure 24. Gaseous volume fraction with a gas volume fraction iso-value of 0.8 for the four different models.

composition results. The same properties for the coal, limestone, and char are used and are given in Table 2. Additional case setups are carried out for the three-dimensional models to compare different gaseous inlet velocities and temperatures to further experimental results from the literature.³² The model conditions and experimental results are given in Table 3.

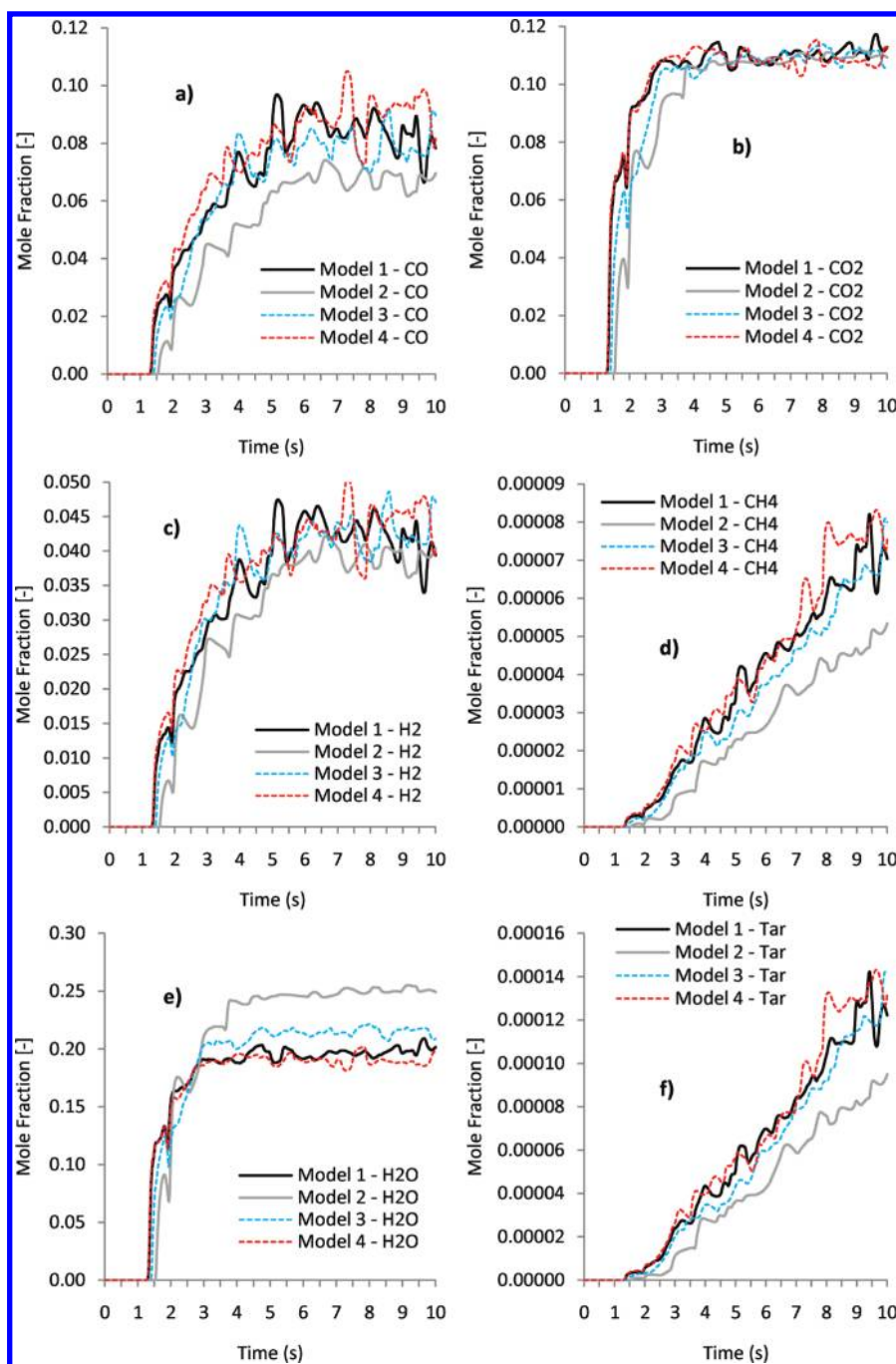


Figure 25. Instantaneous average composition of the individual gaseous species: a) CO, b) CO₂, c) H₂, d) CH₄, e) H₂O, and f) tar for each model.

Gas Inlet Velocity Variation. Three-dimensional models were carried out for models 1, 2, 3, and 4, in Table 3, for 10.0 s which took almost two weeks on 8 processors using a time step of 0.0005 s. The gas distribution within the four beds are given in Figure 24. Iso-values for a gaseous volume fraction of 0.8 are visible displaying the presence of the bubble in their irregular distorted shapes at different positions within the reactor.

Typical characteristics can be seen in all three models including the formation of gases near the fuel inlet due to the build up of volatile gases, the elongation of bubbles near the walls, the formation of endogenously formed bubbles resulting from the heterogeneous reactions at the base of the reactor, and the eruption of

bubbles at the top of the bed. The bubbles appear to be larger with increasing height as coalescence takes place - particularly seen in case 4 of Figure 24 where bubbles are in the process of merging. Although the velocity of the inlet gases vary the bubbles appear to display similar bubble diameters. It is hard to determine whether this is just what appears at this particular instant or whether the bubbles are generally of a similar diameter. However the inlet velocities do not vary a great deal; therefore, it can be assumed that the bubble diameters would be relatively similar.

The instantaneous composition of the individual gaseous species taken and averaged from the outlet for each model are given in Figure 25. The first observation is that the species CO,

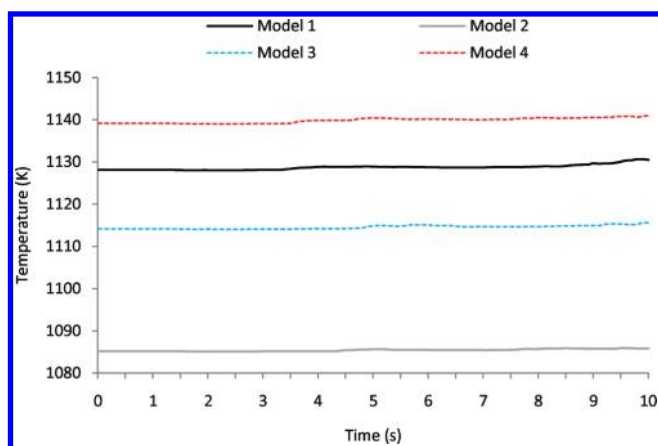


Figure 26. Instantaneous average gas temperature for each model taken at the exit of the reactor.

CO_2 , H_2 , and H_2O display steady compositions after about 5.0 s, whereas CH_4 and tar do not. This is expected because the amount of CH_4 and tar present is very small and continually build up following the devolatilization process. The tar is building up due to the devolatilization alone as it does not participate in any further reactions. On the other hand, CH_4 is a reaction of the oxidation reaction (R7) and is the product of the methanation reaction (R4). However it was shown previously³⁴ that these two reactions take place very slowly, and closer inspection of Figure 25 (d) and (f) shows that the CH_4 and tar graphs look almost identical with regards to the peaks and troughs. This suggests that regardless of the reactions that CH_4 participates in they are negligible as the main contribution to the production of CH_4 as its production is the same as that for the tar, namely from the devolatilization process.

Model 1 and model 4, in Figure 25, display similar magnitudes which is quite expected since their model setups are almost identical except for an increase in bed and inlet temperatures. Therefore any variation between these two models would be a result of temperature differences. Figure 26 displays the average temperature of the gases leaving the reactor over the 10.0 s period, and there is a clear difference due to the initial temperature setups. The temperature trends in Figure 26 appear to replicate the mole fractions of the individual gaseous species in Figure 25. The mole fractions of CO , H_2 , CH_4 , and tar appear to increase with increasing temperatures, while the mole fraction of H_2O shows a decrease with increasing temperatures. The reason for the CH_4 and tar increases with increasing temperature is due to the strong temperature dependence of the devolatilization model; therefore, the higher the bed temperature, the faster the rate of volatile release leading to a faster accumulation of the respective species. The reason for the increase in mole fraction of CO and H_2 and decrease of H_2O with temperature is due to the effects that temperature has on the heterogeneous reactions. Similarly with the devolatilization reactions, the heterogeneous reactions are strongly temperature dependent; therefore, the reactant of the steam gasification reaction (R2), H_2O , would be consumed faster leading to the reduction in this species with increasing temperature. The products of this reaction, CO and H_2 , would be produced faster leading to an increase in their mole fraction with increasing temperature.

The average mole fraction of CO_2 does not show a definitive increase or decrease in mole fraction with increasing temperature. CO_2 is the product of the dominant combustion reaction

Table 5. Temperature Increases from Average Temperature Taken at the Beginning and at the End of the Simulation

temperature (K)	model 1	model 2	model 3	model 4
at 0.0 s	1128.15	1085.15	1114.15	1139.15
at 10.0 s	1130.5116	1085.8207	1115.6143	1141.0187
increase	2.3616	0.6707	1.4643	1.8687

(R1); therefore, increasing the temperature would produce CO_2 much faster. It appears from Table 3 that the ratio of air to steam increases with increasing bed temperatures; therefore, with higher temperatures there is more O_2 available for consumption through the combustion reaction leading to an increase in CO_2 . Furthermore, CO_2 is one of the dominant species of the devolatilization process; therefore, CO_2 would also be supplied faster from the fuel inlet. Therefore it would be assumed that the mole fraction of CO_2 would increase with increasing temperature. This can be seen in the initial stages of Figure 25 b); however, after about 4.0 s the mole fractions for all models do not show any distinctive variation between the different models. CO_2 is also the reactant of the Boudouard reaction (R3), so any additional CO_2 with increasing temperatures would promote this reaction leading to an increase in CO , as was observed. Therefore, while CO_2 is being produced faster with increasing temperatures it is also being consumed faster leading to the similar average composition between the models.

Figure 26 shows a gradual increase in the average temperatures of the gas leaving the reactor. Table 5 provides the temperature increase from the temperatures taken at the beginning and the end of the 10.0 s simulation. Although the highest temperature does not have the largest temperature increase, the results seems to suggest higher temperatures result in larger temperature increases. This is because an increase in the temperature would lead to an increase in the water-gas shift reaction rate. Since this reaction is slightly exothermic, increased activity would gradually increase the temperature in the freeboard. The water-gas shift reaction is also dependent on the concentration of its reactants, so a possible reason for the slightly higher increase in temperature in model 1 compared to model 4 could be due to a distinctive variation in the mole fraction of the relevant reactants, namely CO , CO_2 , H_2 , and H_2O , between the two models which is seen in Figure 25.

At around 9.5 s there is a large difference between the mole fractions of CO and H_2 for the two models moreover, model 1 there shows a stronger drop in these mole fractions compared to any other previous times. This change in mole fraction would affect the water-gas shift reaction significantly as the species compete to reach equilibrium hence accelerating the equilibrium reaction leading to the generation of more exothermic heat. This would explain the sudden jump in the instantaneous average temperature in Figure 26 around this time for model 1 and hence the slight increase in temperature of this model compared to model 4 at 10.0 s which was seen in Table 5.

Since the majority of the species in Figure 25 appear to display relatively steady compositions after 5.0 s, the mole fraction of the exiting gases were averaged over the final 5.0 s and compared to the relevant experimental data given in the literature³² in Figure 27. In all cases the species show similar trends to the experimental results. Model 3 and model 4 provide close representations of the experimental data for the majority of the species. As expected CH_4 is significantly lower in all cases since it continues to increase in concentration with time as seen previously. The mole fraction of CO_2 shows a

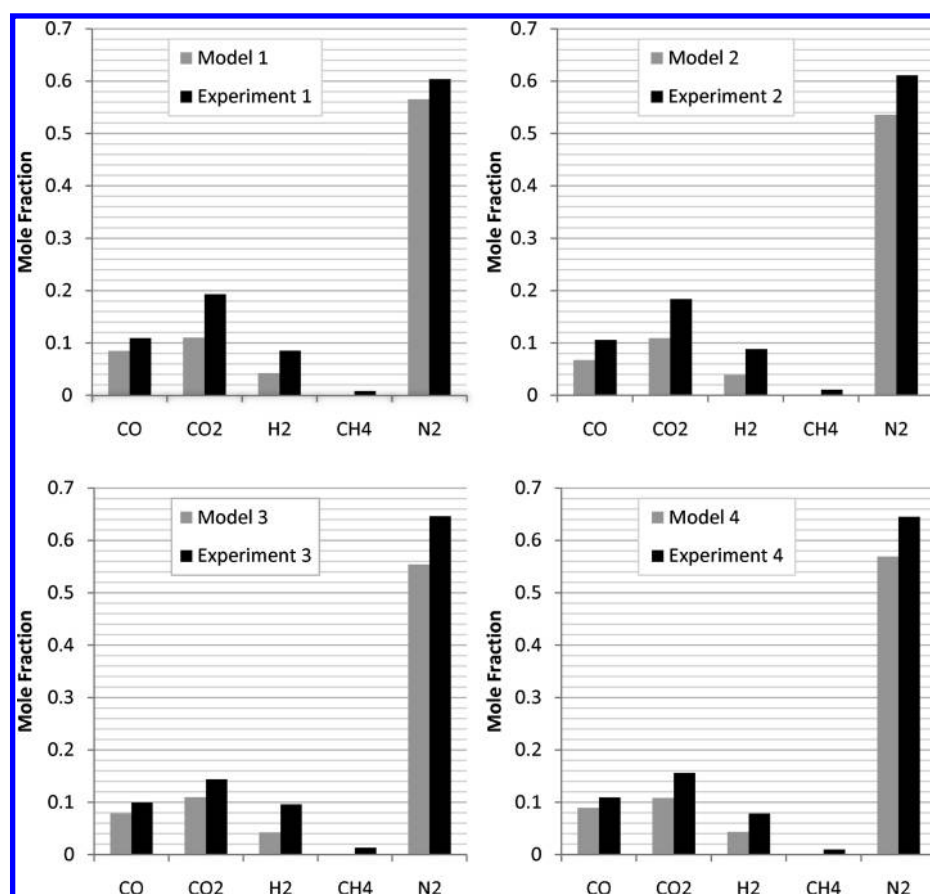


Figure 27. Average mole fraction of the exiting gases for the four different models.

Table 6. Comparison of the Simulated and Experimental Mole Fraction of the Exiting Gases for the Four Different Models

	CO	CO ₂	H ₂	CH ₄	N ₂	H ₂ O	tar
model 1	0.08503	0.11023	0.04261	0.00006	0.56551	0.19647	0.00009
experiment 1	0.10940	0.19310	0.08530	0.00840	0.60370	not given	not given
model 2	0.06748	0.10906	0.03898	0.00004	0.53538	0.24900	0.00007
experiment 2	0.10590	0.18380	0.08840	0.01070	0.61100	not given	not given
model 3	0.07904	0.10987	0.04230	0.00005	0.55385	0.21480	0.00009
experiment 3	0.09970	0.14400	0.09630	0.01340	0.64620	not given	not given
model 4	0.08919	0.10833	0.04350	0.00006	0.56919	0.18963	0.00010
experiment 4	0.10940	0.15600	0.07880	0.01010	0.64520	not given	not given

significant underprediction for model 1 and model 2. Assumptions have been made on the amount of limestone in the bed compared to char, as specific information was not provided in the literature; therefore, this would lead to variations in the predicted results. All the species underpredict the experimental data which are expected as H₂O was found in the simulated results to constitute the largest fraction of the exiting gases and the information for this species was not available in the literature for the experimental results, similarly with the tar information. Therefore if this fraction were to be considered in the experimental data, then the experimental values would decrease which would potentially lead to an improvement in the comparison with the simulated results. For a closer comparison of the average mole fractions of the species the simulated and experimental data are also provided in Table 6. While these results appear to give reasonable good representations, an increasing the time the

results were averaged would give a much better representation of the results.

CONCLUSION

An Eulerian-Eulerian model was carried out on a coal bubbling fluidized bed gasifier for a char and limestone bed with the inclusion of limestone calcination. The composition of the gaseous species for a base case was validated with experimental data from the literature. Finally, different parameters were varied to determine their influence on the gaseous composition of the exiting products.

The results highlighted the simulations sensitivity to different reaction kinetics, i.e., devolatilization models, as well as the variations in experimental setup. The compositions of the bed material, variation of the bed height, temperature of the bed, and the inclusion

of heat transfer coefficients strongly influenced the compositions of the exiting gas emissions.

Increased char levels in the bed and increasing bed temperatures promoted the highly temperature dependent heterogeneous reactions resulting in a faster consumption of their reactants and increased production of their products. Increasing the bed height also led to increased char levels in the bed causing increases and decreases in the concentration of the heterogeneous reactions products and reactants, respectively. However, increasing the bed height also led to a reduced freeboard area which prevented the reactants of the water-gas shift reaction to reach equilibrium effectively.

Heat transfer coefficients on the walls showed that convective transport of heat within the freeboard affected the average gaseous temperature leaving the reactor but did not influence the mole fraction of the gaseous species. This was because the temperature of the bed dominates over the heat transfer coefficient that are local to the walls.

Two models were carried out for a limestone only bed, one treating the limestone as inert while the other calcinated. The results showed that the contribution of additional CO₂ through calcination was only small. The results also showed very low composition of all the species as the only char taking place in heterogeneous reactions was that produced as a product of devolatilization. Lower char concentrations led to more O₂ which enabled the oxidation homogeneous reactions to consuming the products of devolatilization and heterogeneous reactions immediately.

Extended simulation times showed steady gaseous compositions were achieved after approximately 400.0 s suggesting that previous coal gasification results obtained both presently and in the literature^{31,33,34} which ran up to 100.0 s, ran for an insufficient period of time.

The mass of the solid phases were analyzed showing a reduction in char due to heterogeneous reaction and an increase in coal which leveled off as the bed became accustomed to the introduction of fresh coal and the consumption due to the devolatilization processes. The limestone showed a gradual increase due to a constant inflow of limestone in the fuel inlet. Its constituents, CaCO₃ and CaO, showed a decrease and increase, respectively, due to the calcination reaction.

Three-dimensional models were also carried out which tested different gas inlet velocities and temperatures and agreed reasonably well with experimental data from the literature.

The current model only contains four heterogeneous reactions, four homogeneous reactions, and the influence of limestone calcination alone. It would be interesting to extend the available reactions that are taking place, especially those involved with NO_x and SO_x modeling. Furthermore, should SO_x modeling be included then limestone desulfurization can also be considered.

AUTHOR INFORMATION

Corresponding Author

*E-mail: s.gu@soton.ac.uk.

ACKNOWLEDGMENT

The authors gratefully acknowledge the financial support from UK EPSRC Grant EP/G034281/1, and Leverhulme-Royal Society Africa Award.

REFERENCES

(1) Berruti, F.; Chaouki, J.; Godfroy, L.; Pugsley, T.; Patience, G. Hydrodynamics of circulating fluidized bed risers: a review. *Can. J. Chem. Eng.* **1995**, *73* (5), 579–602.

(2) Samuelsberg, A.; Hjertager, B. An experimental and numerical study of flow patterns in a circulating fluidized bed reactor. *Int. J. Multiphase Flow* **1995**, *22*, 575–591.

(3) Benyahia, S.; Arastoopour, H.; Knowlton, T.; Massah, H. Simulation of Particles and Gas Flow Behaviour in the Riser Section of a Circulating Fluidized Bed using the Kinetic Theory Approach for the Particulate Phase. *Powder Technol.* **2000**, *112*, 24–33.

(4) Almuttahir, A.; Taghipour, F. Computational fluid dynamics of high density circulating fluidized bed riser: Study of modeling parameters. *Powder Technol.* **2008**, *185*, 11–23.

(5) Goldschmidt, M.; Kuipers, J.; van Swaaij, W. Hydrodynamic modelling of dense gas-fluidized beds using the kinetic theory of granular flow: effect of restitution coefficient on bed dynamics. *Chem. Eng. Sci.* **2001**, *56*, 571.

(6) Armstrong, L.-M.; Luo, K.; Gu, S. Two-dimensional and Three-dimensional Computational Studies of Hydrodynamics in the Transition from Bubbling to Circulating Fluidised Bed. *Chem. Eng. J.* **2010a**, *160*, 239–248.

(7) Patil, D.; Smit, J.; van Sint Annaland, M.; Kuipers, J. Wall-to-bed Heat Transfer in Gas-Solid Bubbling Fluidized Beds. *AIChE J.* **2006**, *52*, 58–74.

(8) Schmidt, A.; Renz, U. Numerical prediction of heat transfer in fluidized beds by a kinetic theory of granular flows. *Int. J. Therm. Sci.* **2000**, *39*, 871–885.

(9) Kuipers, J.; Prins, W.; van Swaaij, W. Numerical calculation of wall-to-bed heat transfer coefficients in gas-fluidized beds. *AIChE J.* **1992**, *38*, 1079–1091.

(10) Armstrong, L.-M.; Luo, K.; Gu, S. The influence of multiple tubes on the tube-to-bed heat transfer in a fluidised bed. *Int. J. Multiphase Flow* **2010**, *36*, 916–929.

(11) Gera, D.; Gautam, M.; Tsuji, Y.; Kawaguchi, T.; Tanaka, T. Computer simulation of bubbles in large-particle fluidized beds. *Powder Technol.* **1998**, *98*, 38–47.

(12) Gera, D.; Syamlal, M.; O'Brien, T. Hydrodynamics of particle segregation in fluidized beds. *Int. J. Multiphase Flow* **2004**, *30*, 419–428.

(13) Ibsen, C.; Helland, E.; Hjertager, B.; Solberg, T.; Tadriss, L.; Occelli, R. Comparison of multifluid and discrete particle modelling in numerical predictions of gas particle flow in circulating fluidised beds. *Powder Technol.* **2004**, *149*, 29–41.

(14) Papadikis, K.; Bridgwater, A.; Gu, S. CFD modelling of the fast pyrolysis of biomass in fluidised bed reactors. Part A: Eulerian computation of momentum transport in bubbling fluidised beds. *Chem. Eng. Sci.* **2008**, *63* (16), 4218–4227.

(15) Papadikis, K.; Gu, S.; Bridgwater, A. CFD modelling of the fast pyrolysis of biomass in fluidised bed reactors. Part B: Heat, momentum and mass transport in bubbling fluidised beds. *Chem. Eng. Sci.* **2009**, *64*, 1036–1045.

(16) Papadikis, K.; Gerhauser, H.; Bridgwater, A.; Gu, S. CFD modelling of the fast pyrolysis of an in-flight cellulosic particle subjected to convective heat transfer. *Biomass Bioenergy* **2009**, *33* (1), 97–107.

(17) Papadikis, K.; Gu, S.; Bridgwater, A. CFD modelling of the fast pyrolysis of biomass in fluidised bed reactors: Modelling the impact of biomass shrinkage. *Chem. Eng. J.* **2009**, *149*, 417–427.

(18) Papadikis, K.; Gu, S.; Bridgwater, A.; Gerhauser, H. Application of CFD to model fast pyrolysis of biomass. *Fuel Process. Technol.* **2009**, *90*, 504–512.

(19) Papadikis, K.; Gu, S.; Bridgwater, A. Computational modelling of the impact of particle size to the heat transfer coefficient between biomass particles and a fluidised bed. *Fuel Process. Technol.* **2010**, *91* (1), 68–79.

(20) Papadikis, K.; Bridgwater, A.; Gu, S. A CFD approach on the effect of particle size on char entrainment in bubbling fluidised bed reactors. *Biomass Bioenergy* **2010**, *34* (1), 21–29.

(21) Papadikis, K.; Gu, S.; Fivga, A.; Bridgwater, A. Numerical comparison of the drag models of granular flows applied to the fast pyrolysis of biomass. *Energy Fuels* **2010**, *24* (3), 2133–2145.

(22) Papadikis, K.; Gu, S.; Bridgwater, A. 3D simulation of the effects of sphericity on char entrainment in fluidised beds. *Fuel Process. Technol.* **2010**.

- (23) Moreea-Taha, R. *Modelling and simulation for coal gasification* 2000.
- (24) de Souza-Santos, M. Comprehensive modeling and simulation of fluidized bed boilers and gasifiers. *Fuel* **1989**, 68, 1507–1521.
- (25) Chejne, F.; Hernandez, J. Modeling and simulation of coal gasification process in fluidized bed. *Fuel* **2002**, 81, 1687–1702.
- (26) Baum, M. M.; Street, P. J. Predicting the combustion behavior of coal particles. *Combust. Sci. Technol.* **1971**, 3 (5), 231–243.
- (27) Pillai, K. K. The influence of coal type on devolatilization and combustion in fluidized beds. *J. Inst. Energy* **1981**, 142.
- (28) Badzioch, S.; Hawksley, P. G. W. Kinetics of thermal decomposition of pulverized coal particles. *Ind. Eng. Chem. Process Des. Dev.* **1970**, 9, 521–530.
- (29) Stickler, D. B.; Gannon, R. E.; Kobayashi, H. *Rapid devolatilization modeling of coal* 1974.
- (30) Kobayashi, H. *Devolatilization of Pulverized Coal at High Temperatures*. Ph.D. Thesis, Department of Mechanical Engineering, Massachusetts Institute of Technology, Cambridge, Mass, 1976.
- (31) Yu, L.; Lu, J.; Zhang, X.; Zhang, S. Numerical simulation of the bubbling fluidized bed coal gasification by the kinetic theory of granular flow (KTGF). *Fuel* **2007**, 86, 722–734.
- (32) Ocampo, A.; Arenas, E.; Chejne, F.; Espinel, J.; Londono, C.; Aguirre, J.; Perez, J. An experimental study on gasification of Colombian coal in fluidised bed. *Fuel* **2003**, 82, 161–164.
- (33) Wang, X.; Jin, B.; Zhong, W. Three-dimensional simulation of fluidized bed coal gasification. *Chem. Eng. Proc.* **2009**, 48, 695–705.
- (34) Armstrong, L.-M.; Luo, K.; Gu, S. Effects of limestone calcination on the gasification processes in a BFB coal gasifier. *Chem. Eng. J.* **2011**In press.
- (35) Wang, Y.; Lin, S.; Suzuki, Y. Study of limestone calcination with CO₂ capture: decomposition behavior in a CO₂ atmosphere. *Energy Fuels* **2007**, 21, 3317–3321.
- (36) Vasquez, S.; Ivanov, V. A Phase Coupled Method for Solving Multiphase Problems on Unstructured Meshes. 2000.
- (37) Enwald, H.; Peirano, E.; Almstedt, A.; Leckner, B. Simulation of the fluid dynamics of a bubbling fluidized bed experimental validation of the two-fluid model and evaluation of a parallel multiblock solver. *Chem. Eng. Sci.* **1999**, 54, 311–328.
- (38) Johnson, P.; Jackson, R. Frictional-collisional constitutive relations for granular materials, with application to plane shearing. *J. Fluid Mech.* **1987**, 176, 67–93.
- (39) Gerber, S.; Behrendt, F.; Oevermann, M. An Eulerian modeling approach of wood gasification in a bubbling fluidized bed reactor using char as bed material. *Fuel* **2010**, 89 (10), 2903–2917.
- (40) Loison, R.; Chauvin, R. Pyrolyse rapide du charbon. *Chim. Ind.* **1964**, 91, 269.